Journal of Cultural Heritage 67 (2024) 500–511

Contents lists available at ScienceDirect

Journal of Cultural Heritage

journal homepage: www.elsevier.com/locate/culher

Original article

Correlative microscopy and Micro-Raman spectroscopy for enhancing the evaluation of corrosion damage in archaeological objects

Martina Bernabale[a], Flavio Cognigni[b], Silvia Contessi[c], Serena Silvestri[d,e], Giancarlo La Penna[b], Federica Spagnoli[f], Caterina De Vito[a,*], Marco Rossi[b]

[a] Department of Earth Sciences, Sapienza University of Rome, P.le Aldo Moro 5, 00185 Rome, Italy
[b] Department of Basic and Applied Sciences for Engineering (SBAI), Sapienza University of Rome, Via Antonio Scarpa 14, 00161 Rome, Italy
[c] Carl Zeiss S.p.A, Via Varesina, 162, 20156 Milan, Italy
[d] Department of Chemistry, Sapienza University of Rome, P.le Aldo Moro 5, 00185 Rome, Italy
[e] Centro nazionale Sicurezza delle Acque (CeNSiA), Istituto Superiore di Sanità, Viale Regina Elena 299, 00161 Rome, Italy
[f] Department Italian Institute of Oriental Studies - ISO, Sapienza University of Rome, Circonvallazione Tiburtina 4, 00185 Rome, Italy

ARTICLE INFO

Article history:
Received 4 March 2024
Accepted 23 April 2024
Available online 9 May 2024

Keywords:
XRM
HR-FESEM
Iron corrosion
Micro-Raman spectroscopy

ABSTRACT

In this work, we employed correlative imaging techniques to investigate the complex corrosion systems in nails from the Phoenician-Punic site of Motya (Sicily, Italy), combining analytical chemistry and imaging tomography across multiple dimensions and scales. To accomplish this, we used correlative light and electron microscopy, micro-Raman spectroscopy, and X-ray microscopy. The results showed remarkable differences in the condition of the nails, with one nail well-preserved and thinly coated with oxyhydroxides, while the other nail exhibited extensive corrosion and degradation with distinct corrosion layers and the presence of soil minerals. Multiscale X-ray microscopy provided 3D imaging of the internal structures, revealing cracks and the original shape of the nails. This work contributes to the understanding of stress corrosion in metals and has implications for the development of strategies to prevent and control corrosion processes.

1. Introduction

Correlative imaging is a powerful method for investigating complex corrosion systems. It involves the integration of complementary investigation techniques to perform multiscale and multimodal experiments, all focused on the same area of interest [1–4]. This approach is particularly valuable when studying metals and their alloys, which exhibit significant heterogeneity, including the coexistence of multiple phases and the formation of various polymorphs [5–8].

In the context of forging conditions, where metals are subjected to high temperature and pressure and exposed to a corrosive environment, a particular type of corrosion could arise, also known as stress corrosion [9]. This type of corrosion is commonly observed in nails because these objects are typically subjected to high levels of mechanical stress when they are driven into a material, such as wood or concrete. This stress, combined with the presence of a corrosive environment, such as oxygen, moisture, or chemicals present in the surrounding medium, creates ideal conditions for stress corrosion to initiate and propagate. The combination of applied stress and corrosive agents can accelerate the degradation process, leading to the development of cracks and eventual failure of the nail [9,10].

In this study, we utilized an advanced imaging workflow in which fundamental principles were paved in [9] to examine a set of iron nails. In particular, we adopted a combined approach encompassing X-ray microscopy (XRM), correlative light and electron microscopy (CLEM), and micro-Raman spectroscopy. Our correlative strategy involved several key steps, as shown in the flowchart of Fig. 1. Firstly, we employed multiscale XRM, a non-destructive imaging technique that allows for the exploration of internal structures and the reconstruction of 3D volumes of the objects [9–11]. This technique provides highly resolved 3D images, enabling the study of the spatial distribution of different phases, identification of inclusions, and detection of defects within the micro- and nano-meter scale [4,11–22]. It can be particularly valuable in investigating the presence of corrosion products, uncorroded metal-core, and other relevant features. Additionally, we performed a

* Corresponding author.
E-mail address: caterina.devito@uniroma1.it (C. De Vito).

https://doi.org/10.1016/j.culher.2024.04.016

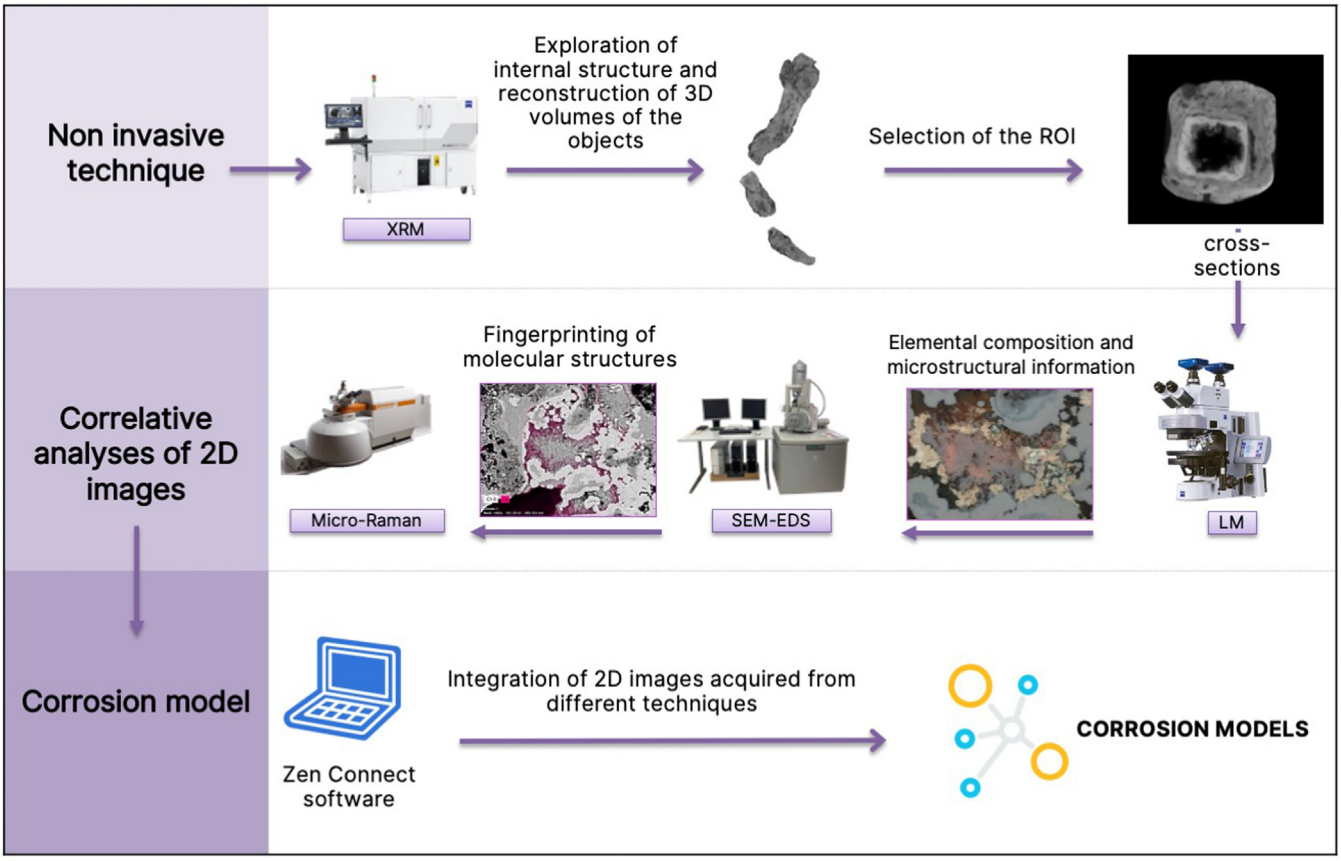

Fig. 1. Flowchart summarizing the correlative workflow employed in this study.

minimum sampling of the artifacts to prepare real cross-sections for examination using CLEM and micro-Raman spectroscopy. CLEM allows for detailed visualization of the corrosion layers from-rim-to-core and permits the study of their chemistry, including the identification of corrosion products and metallic nanostructures. Micro-Raman spectroscopy provides valuable information regarding the bondings within molecular and crystalline structure under investigation, offering a fingerprinting of the corrosion compounds [6,23–25].

2. Research aims

The main objective was to obtain comprehensive information about the microstructure, composition, and any changes resulting from stress corrosion in archaeological iron artifacts. Acquiring such knowledge is of paramount importance for designing effective strategies to prevent and control stress corrosion in materials exposed to forging processes. The application of this analytical approach, carried out on archaeological materials, could similarly be extended to various more durable and corrosion-resistant modern metals. Therefore, precise localization of the region of interest through the implementation of diverse techniques is fundamental in correlative imaging. This approach allows to focus the analysis on specific areas where stress corrosion is likely to manifest, thereby enhancing the accuracy and relevance of the investigations [11,13,16,22,26].

3. Material and methods

3.1. Material

The two iron nails here studied were unearthed in the Phoenician-Punic site of Motya (Sicily, Italy) and date back to the 5th-4th century BC. The ancient city of Motya, located at the heart of the Marsala Lagoon in Trapani on the western edge of Sicily, stands as one of the most significant Phoenician colonies in the central Mediterranean region. It served as a vital maritime center in antiquity, playing a pivotal role in Mediterranean trade and cultural exchange, and facilitating crucial advancements in metal technology. Sample MC.14.08 was discovered embedded in a layer of ash that had been sealed by a pavement. Sample MC.03.43 was unearthed from a votive deposit in the open-air Sanctuary C3. Once discovered, the samples were cleaned, stabilized, and, then, stored in a controlled environment within the storeroom of archaeological finds, where temperature, relative humidity, and light intensity are regulated to prevent any resumption of corrosion and maintain their condition.

3.2. X-ray microscopy (XRM) and dataset reconstruction

XRM was performed using ZEISS Xradia Versa 610 (Carl Zeiss, Oberkochen, Germany) available at Sapienza Nanoscience & Nanotechnology Laboratories (SNN-Lab) of the Research Center on Nanotechnology Applied to Engineering (CNIS) of Sapienza University of Rome. XRM experiments for samples MC.03.43 and MC.14.08 were performed respectively with X-ray source voltage and power of 140 kV and 21 W and 150 kV and 23 W. The pixel size was set to 51.45 µm and 13 µm, 1601 projections were acquired and the 0.4x objective was selected. Datasets were reconstructed using the Feldkamp-Davis-Kress (FDK) cone-beam reconstruction algorithm [27] in ZEISS *Scout-and-Scan Control System Reconstructor* software (Version 16.1.13038.43540, Carl Zeiss, Oberkochen, Germany). 3D models of the samples were investigated and processed using Dragonfly Pro (Version 2022. 1 Build 1259, Object Research Systems, Montreal, Quebec, Canada).

3.3. Light microscopy (LM)

LM observations were performed using a ZEISS Axio Imager (Carl Zeiss, Oberkochen, Germany) equipped with a motorized table, 20×, 50×, 100× objectives and coupled with an AxioCam 503 color available at the Carl Zeiss S.p.A. - Quality Excellence Center, Reggio Emilia, Italy).

3.4. Scanning electron microscopy (SEM) and energy dispersive X-ray spectroscopy (EDX)

SEM and EDX investigations were performed using a ZEISS EVO 15 (Carl Zeiss GmbH, Oberkochen, Germany) equipped with Ultim Max 65 mm^2 (Oxford Instruments, Abingdon-on-Thames, United Kingdom) EDX probe available at the Carl Zeiss S.p.A. - Quality Excellence Center (Reggio Emilia, Italy). SEM images and EDX spectra/maps were acquired using the following parameters: acceleration voltage 25 kV, probe current 300 pA, aperture size 30 μm, WD 8.5 mm.

3.5. Correlative light and electron microscopy (CLEM)

LM, SEM and EDX experiments as well as image alignment and visualization were performed in a correlative microscopy environment provided by ZEISS ZEN Connect software (Carl Zeiss, Oberkochen, Germany).

3.6. μ-Raman spectroscopy

Micro-Raman analyses were performed at room temperature using an inVia™ confocal Raman spectrometer (Renishaw) with a focal length of 250 mm. The 1800 l/mm holographic diffraction grating and the Peltier cooled CCD detector were used. The samples were excited using two different excitation line lasers: an Nd:YAG (Renishaw) continuous-wave diode-pumped solid-state laser with a wavelength of 532.1 nm (green laser) and an output power of 50 mW and a Renishaw HeNe laser with a wavelength of 632.816 nm (red laser) and output power of 17.5 mW. The laser beam was focused onto the samples using a 50 × short working-distance N-Plan objective (N.A. = 0.75, Leica Microsystems). In addition, in the case of green laser analysis, a 5 x long working-distance N-Plan objective (N.A. = 0.12, Leica Microsystems) and a 20x short working-distance N-Plan objective (N.A. = 0.4, Leica Microsystems) were also employed.

For measurements conducted with the 633 nm laser (red laser) the signal was acquired within the 150–1350 cm^{-1} spectral range, as depicted in Fig. 5. The laser beam was focused to a spot diameter of approximately 1 µm using a 50x objective lens, and the spectra were obtained with the laser power set at 10 % (approximately 1.75 mW) relative to the nominal power value.

Conversely, for measurements performed with the 532 nm laser, as shown in Fig. 8a, the spectral acquisition range was 180–1940 cm^{-1}. A laser beam with a spot diameter of around 1.6 µm was utilized through a 20× objective lens, with the spectra collected at a laser power of 5 % (approximately 2.5 mW) compared to the nominal power value. Additionally, the spectra presented in Fig. 8b–d were captured using a laser beam with a spot diameter of approximately 0.9 µm through a 50x objective lens, with the spectra collected at a laser power of 5 % (approximately 2.5 mW) relative to the nominal power value. Furthermore, measurements conducted with the green laser resulted in the acquisition of the quartz spectrum depicted in Fig. 8e using a laser beam with a spot diameter of approximately 5.4 µm through a 5× long-working distance objective lens. The spectrum was collected at a laser power of 50 % (approximately 25 mW) compared to the nominal power value.

All spectra are acquired with an exposure time of 1 s and an average of 30 accumulations.

All the post-processing activities (normalization, smoothing, peak label) have been carried out on the software WiRE™ 4.4; normalized intensities of each band result from the ratio of their height and one of the most intense peaks of the spectrum and peak positions were calibrated using both internal and external silicon references.

4. Results

4.1. 3D imaging of internal structures by XRM

XRM was used to investigate the three-dimensional phase distribution and stress corrosion mechanisms in a non-destructive way. In 3D tomography imaging, the grey scale levels are related to the absorption coefficient of the material being imaged, as well as the length of the X-ray beam path through the sample. The absorption coefficient determines the X-ray intensity absorbed by the material, which affects the intensity of the X-rays reaching the detector. The metal core has a higher absorption coefficient than the surrounding corrosion layers, appearing as a lighter shade of gray in the reconstructed dataset, while the corrosion layers appear as a darker shade of gray. Nail MC.03.43 features a tapered square cross-section stem with a 120° bent tip. The formation of cracks oriented along the length of the object is a common phenomenon observed in materials that have been subjected to repeated mechanical stress during the forging process. The square cross-section of the nail was likely forged by orthogonal hammering, which involved striking the metal at right angles to produce a symmetrical shape.

The digital alignment of the fragments of the nail, measuring 6.4 cm in length overall, allowed us to accurately reconstruct the original shape of the nail and observe the pattern and dimensions of cracks, which measure approximately 5 mm in length. By studying the distribution and orientation of the cracks, it is possible to gain insight into the manufacturing techniques and use the history of the nail. After being subjected to several and multi-directional forces, at the end of the forging, the central area appears weak, fully corroded, and hollow (Fig. 2, Video 1).

Another important achievement is the ability to recognize and localize the position of the original shape (OS) of the nail using X-ray microscopy (XRM), even beneath layers of corrosion products. The limit of the original surface (LIMITOS) is defined as the boundary between the surface of the object and the surrounding soil before the onset of the corrosion process [28,29]. However, more precisely, what is observed in Fig. 2d is the difference between the dense product layer (DPL), under the original surface and outer corrosion products, also known as transformed medium (TM). This is because, during corrosion processes, the LIMITOS may not align with the original level of the object and can shift during the formation of oxide scales. Through a histogram-based thresholding approach, the internal core of the nail was segmented and isolated from the rest of the object. The artifact's surface was exported as a triangle mesh file (i.e., an ensemble of vertices, edges and faces that compose the shape of a polyhedral object) and visualized as a solid transparent element. The segmented core across the three parts of the nail (green, pink, red,) was displayed revealing its spatial arrangement within the sample volume, as depicted in Fig. 2.

Conversely, nail MC.14.08 is characterized by a small, flattened round head and circular section stem. It shows a homogeneous and well-preserved iron core from the head down to the tip and a thin external corrosion layer (Fig. 3), suggesting that the nail was well-protected from external forces and environmental factors. This may have been due to differences in the manufacturing process or use

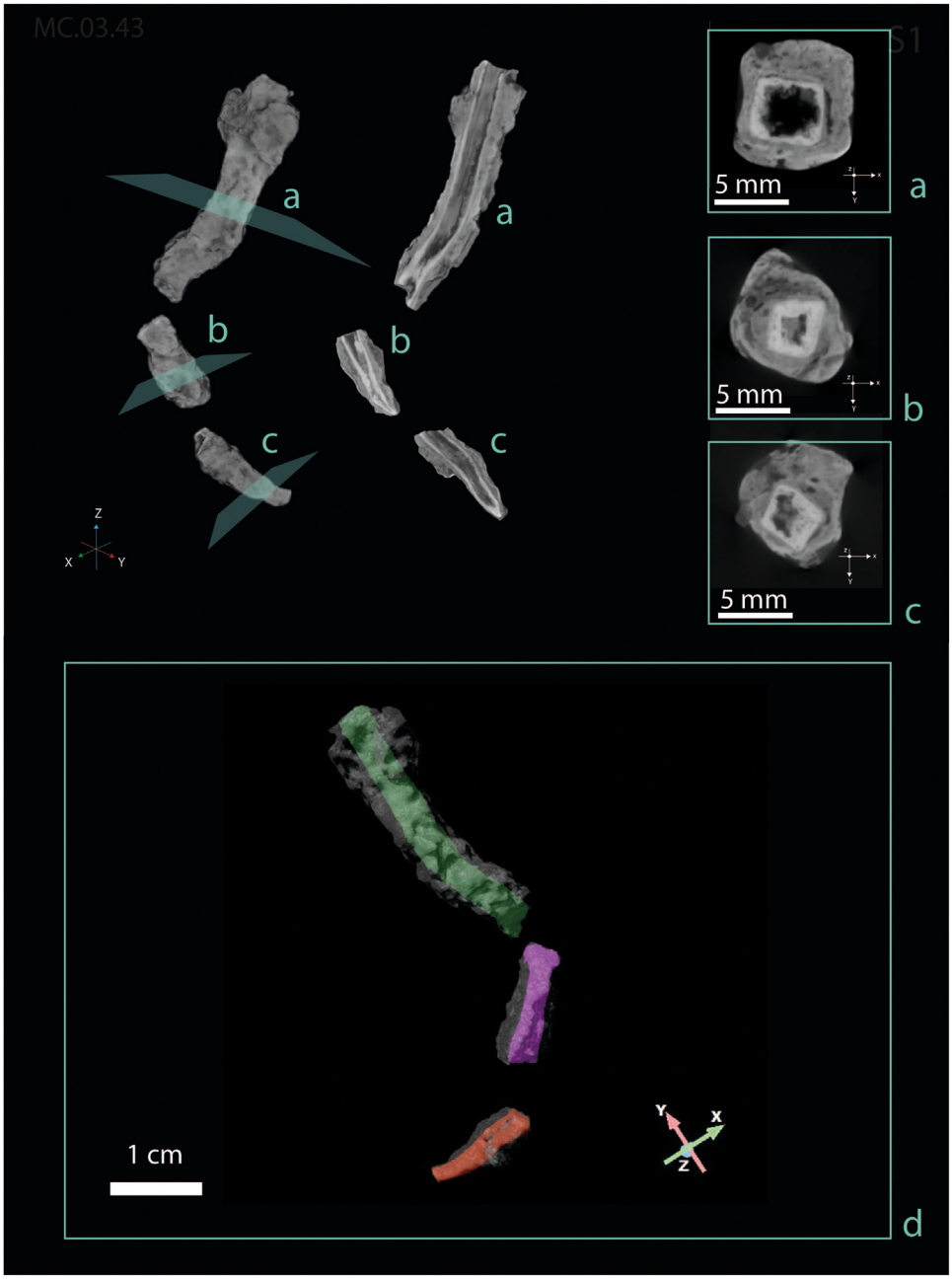

Fig. 2. (a,b,c) 3D reconstruction of three fragments of the nail MC.03.43 and virtual sections (S1, S2 and S3) corresponding to the top, the middle, and the tip of the nail. (d)Localization of the limit of the original surface of the nail.

history of the nail, such as a protective coating or limited exposure to moisture or other corrosive substances.

4.2. Correlation of 2D images from cross-sections for elemental and mineralogical composition

The implementation of a multiscale and multimodal correlative light and electron microscopy (CLEM) workflow, facilitated by advanced software such as ZEISS ZEN Connect, allows for the integration of 2D images acquired using different characterization tools. This approach enables the marking of specific sub-regions or features of interest from the object's cross-section, for subsequent alignment and visualization in a unified context. Through chemical analysis conducted using SEM-EDX, we determined that both nails are primarily composed of iron. Sample MC.14.08 consists of wrought iron, predominantly composed of ferrite (99.3 % Fe), with minor amounts of Mn (0.5 wt%) and Si (0.2 wt%) dissolved within the solid solution.

By examining the samples using CLEM, remarkable differences can be observed in the condition of the two nails. Specifically, MC.14.08 appears to be well-preserved, with an uncorroded iron core that is thinly coated with oxyhydroxides (Fig. 4a). Notably, the external layer of MC.14.08 displays distinct Raman bands indicative of the coexistence of goethite (α-FeO(OH)) and lepidocrocite (γ-FeO(OH)). Goethite is identified by its characteristic main peaks at approximately 299 cm^{-1} and 386 cm^{-1} [24,30] (Fig. 5, spectra a, b). However, the occurrence of a peak at around 250 cm^{-1} suggests the presence of lepidocrocite, indicating an ongoing corrosion process [24,30] (Fig. 5a). Additionally, the presence of sporadic regions of magnetite (Fe_3O_4) is detected, as evidenced by a peak around 668 cm^{-1} [24]. At the position of fracture, an orange phase enriched in Cl can be observed, as shown in Fig. 4.

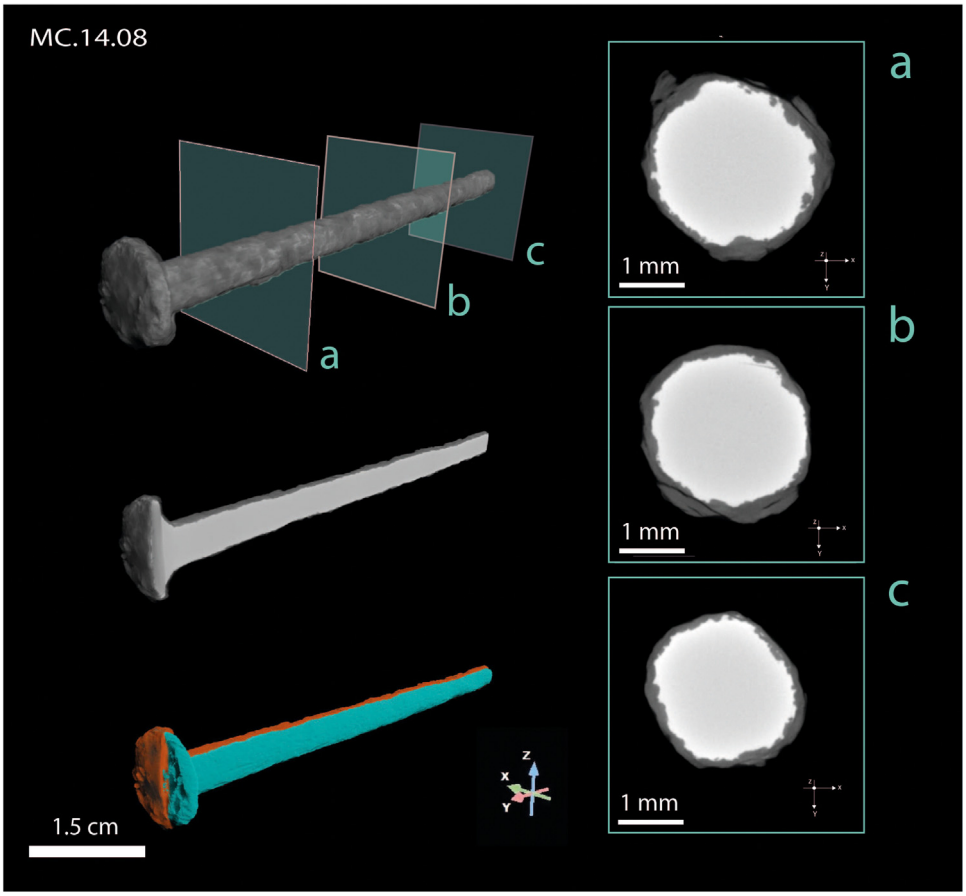

Fig. 3. 3D reconstruction and sagittal section of iron nail MC.14.08 with three different virtual slices and segmentation of the nail showing different layers: orange—corrosion layer, blue—metal.

CLEM and micro-Raman analysis of MC.03.43 reveals that the nail is made of wrought iron but shows a distinct corrosion pattern and conservation condition compared to MC.14.08. Indeed, MC.03.43 shows two distinct corrosion layers: the dense product layer (DPL) and the transformed media (TM) (Fig. 6). The DPL demonstrates characteristic porous structures (Fig. 6a) and consists of corroded iron phases, indicating extensive corrosion and degradation of the nail in specific regions and do not contain any quartz grains. The investigations realized on the corrosion products concern mainly the DPL, reveal a light–dark phase under a light microscope and SEM (Fig. 6b). This phase exhibits a marbled appearance due to the presence of numerous fine, light gray filaments, which are composed of magnetite [28].

The TM layer in MC.03.43 consists of an encrustation coating that includes sand particles and other silicates (Fig. 7a). X-ray maps in Fig. 7b show mainly precipitated iron corrosion phases intermixed with elements originating from the surrounding soil, such as calcium (Ca) and silicon (Si). This suggests that the nail underwent corrosion in a soil environment, resulting in the incorporation of soil elements into the corrosion products [9,29].

Micro-Raman spectra obtained from MC.03.43 provide insights into the identification of different minerals. Like MC.14.08, goethite, lepidocrocite, and magnetite [31] are identified (Fig. 8, spectrum a,b,c). However, the spectra also reveal a complex mixture of soil minerals, such as microcline, calcite, and quartz, embedded within the sample during the degradation process of the nail. Microcline ($KAlSi_3O_8$) is identified through characteristic peaks at 291, 416, 478, and 507 cm^{-1} (Fig. 8, spectrum d). The carbonate group in carbonate-minerals is characterized by a strong band at approximately 1086 cm^{-1} and at 711 cm^{-1} (Fig. 8, spectra b,c) [30,32,33]. Additionally, the Raman peaks at 206 and 465 cm^{-1} confirm the presence of quartz (Fig. 8, spectrum e) [30].

CLEM images of the section reveal that the presence of calcite is associated with environmental depositions and corrosion defects. Indeed, the secondary calcite crystals are attributed to the precipitation of carbonate from subterranean waters rich in calcium carbonate and bicarbonate that fill internal gaps or cracks in the iron structure during the burial process (Fig. 9) [34,35]. Thus, the precipitated calcite is primarily concentrated in areas where water can easily infiltrate.

The different state of conservation of the two iron nails could be traced back to the two contexts characterized by different soils. The first one, MC.14.08, was found within an ashy layer sealed by a pavement, and therefore a layer characterized by alkaline and protective properties. The second one, MC.03.43, was found in a votive deposit of the open-air Sanctuary C3, in a clayish layer and more exposed to atmospheric agents.

5. Discussion

The correlative microscopy approach applied in this research combined the initial survey of samples via XRM coupled with CLEM and chemical information from EDX. The methodological effort provided a comprehensive understanding of both samples. In this context, XRM is a valuable tool to drive further investigation steps. Indeed, non-destructive 3D imaging provides a multiscale overview of the internal and hidden details of an object. Information extracted from the analysis of the 3D dataset is useful for locating specific regions of interest (ROIs) to be investigated at higher resolution or through complementary techniques. When

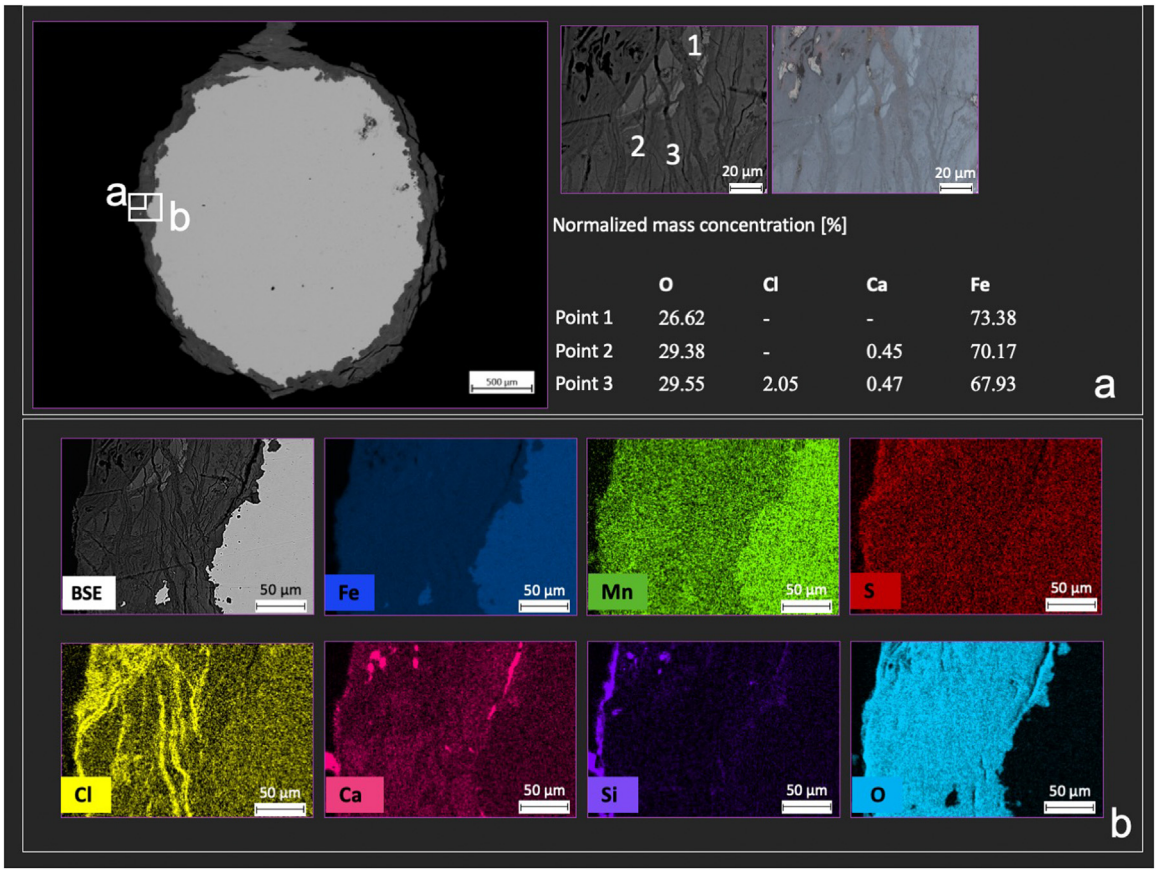

Fig. 4. (a) Correlation of LM, SEM images of corrosion layer in nail MC.14.08 and location of targeted ROI for LM and SEM–EDS imaging and analysis. (b) X-ray maps of Fe, Mn, S, Cl, Ca, Si, and O.

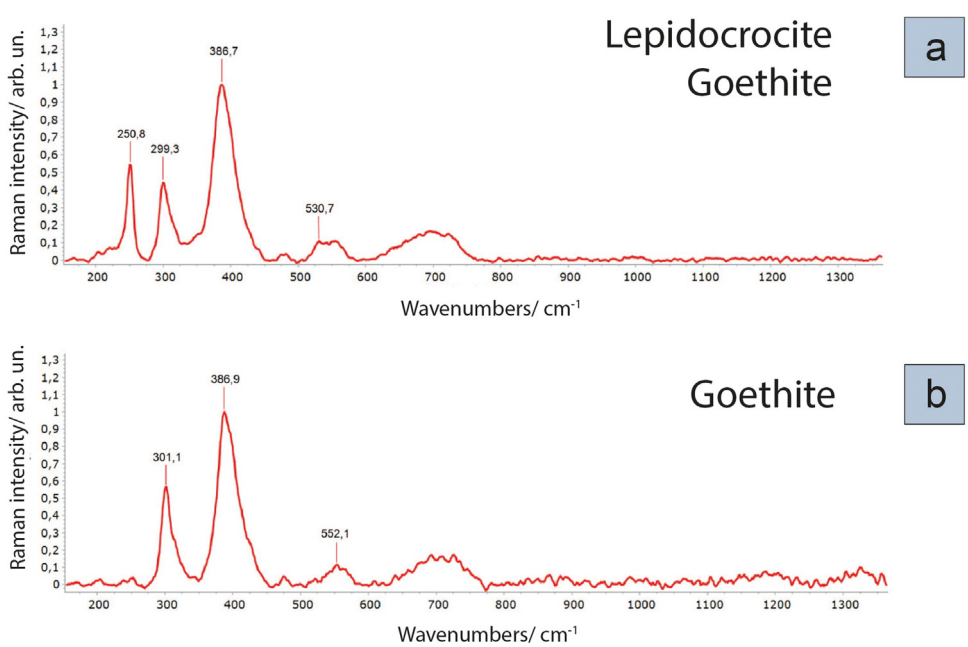

Fig. 5. Raman spectra of sample MC.14.08 (a) lepidocrocite and goethite, (b) goethite.

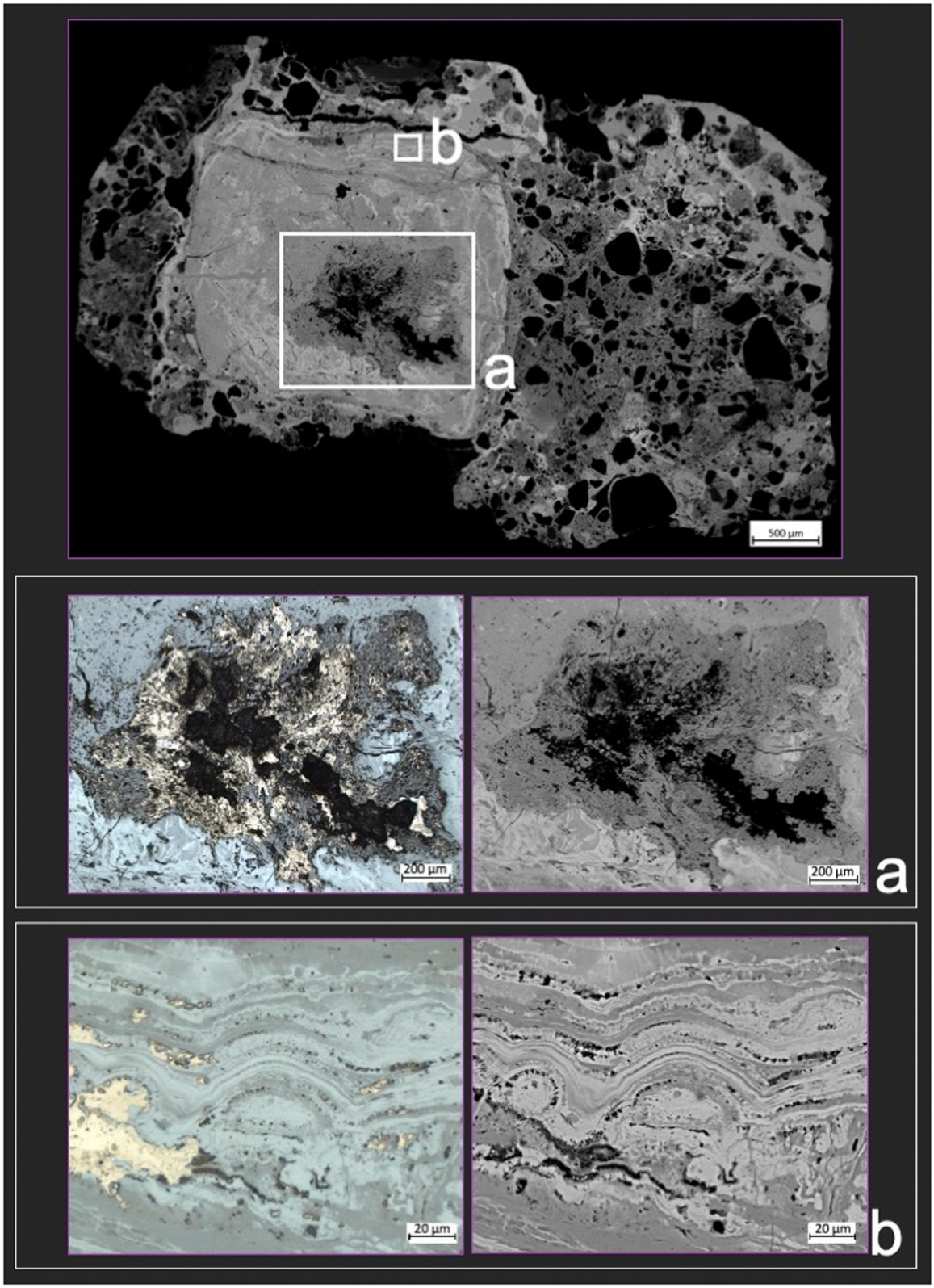

Fig. 6. (a) Correlation of LM, SEM images of porous structures in DPL of nail MC.03.43 (b) LM and SEM detail of marbled-like DPL with the presence of numerous light grey filaments of magnetite.

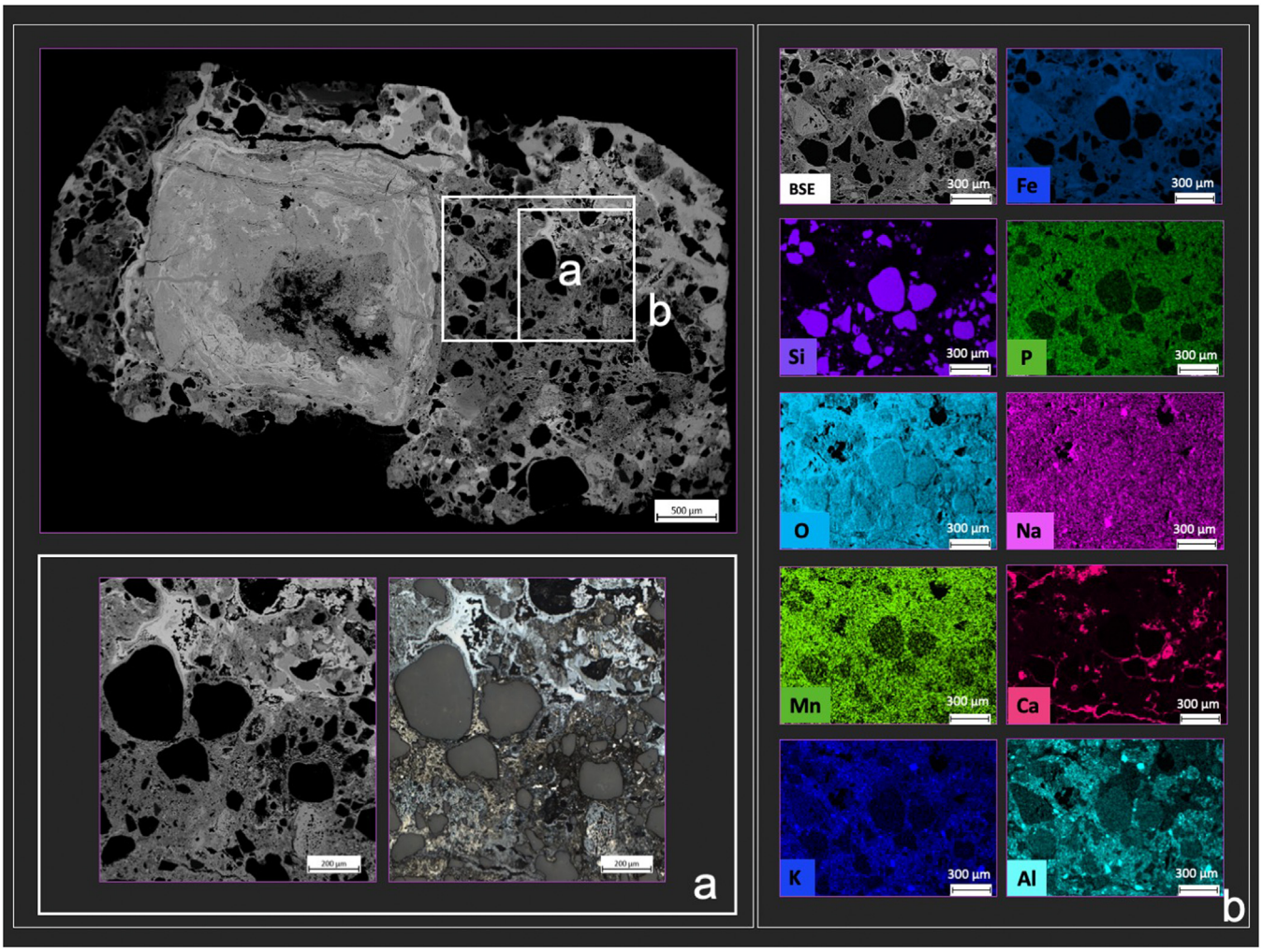

Fig. 7. (a) Correlation of LM, SEM images of TM including sand particles and other silicates in nail MC.03.43 (b) SEM and X-ray maps of Fe, Si, P, O, Na, Mn, Ca, K, Al.

exploiting a correlative light and electron microscopy (CLEM) approach, this knowledge is crucial to determine the ROI in correspondence of which performs the cut to obtain a real-cross section, extracting the maximum information from the specimen. The process should be driven by the need to select an ROI which is a representative portion of the entire sample.

Considering the results of cross-section corrosion characterization and combining them with the structural information obtained with XRM on the entire artifacts, some models on possible corrosion processes can be schematized based on mechanisms already proposed in the literature [36–38]. The comparison between two wrought iron nails reveals a very different evolution of corrosion depending upon a combination of factors, including the soil composition, the level of corrosion, the internal structure of the nail, and the formation of specific iron compounds during the corrosion process. In model A of Fig. 10, nail MC.03.43 experienced extensive plastic deformation during its production that caused thermal residual stresses and therefore enhanced the initiation of the internal crack during the long corrosion process. The internal crack follows the deformation lines created during the hot-working manufacturing process, revealing the original square shape of the nails MC.03.43. Indeed, the interaction of the material with the environment can also play an important role after the formation of the fracture, that is, the crack propagation phase. The occurrence of the internal cavity represents another front of access for oxygen and moisture in the artifact, giving rise to the oxidation of the metal from core to outer soil with the formation of a denser interface (probably maghemite and magnetite) between the more porous layers called transformed medium (TM) that presents soil compounds mixed with iron corrosion products [23,39].

Conversely, nail MC.14.08 in model B has a circular cross-section and shows an excellent state of preservation, revealing an uncorroded metal core and a bi-layer structure.

An interesting aspect to note relates to the presence of chlorine in both iron nails, MC.03.43 and MC.14.08 (see elemental map in Fig. 4b). The primary reason why chlorine tends to concentrate within the fractures in the MC.14.08 nail is linked to chemical interactions and the surface charge of minerals such as iron oxides and oxyhydroxides in the presence of hydroxide ions (OH^-). Under alkaline conditions, these hydroxide ions can adsorb onto the surface of minerals, creating a negative surface charge. This negative charge can repel other negative ions, such as chloride (Cl^-), thereby reducing the likelihood of interaction between chloride and the mineral surface.

Therefore, when chloride is present in the environment, its interaction with the mineral surface is diminished due to electrostatic repulsion generated by the negative charge. Consequently, chloride tends to concentrate within fractures or areas less influenced by the negative surface charge, resulting in a higher chlorine concentration in those areas. The more corroded MC.03.43 nail suggests prolonged exposure to corrosive environmental conditions. Corrosion can lead to the formation of oxidation products

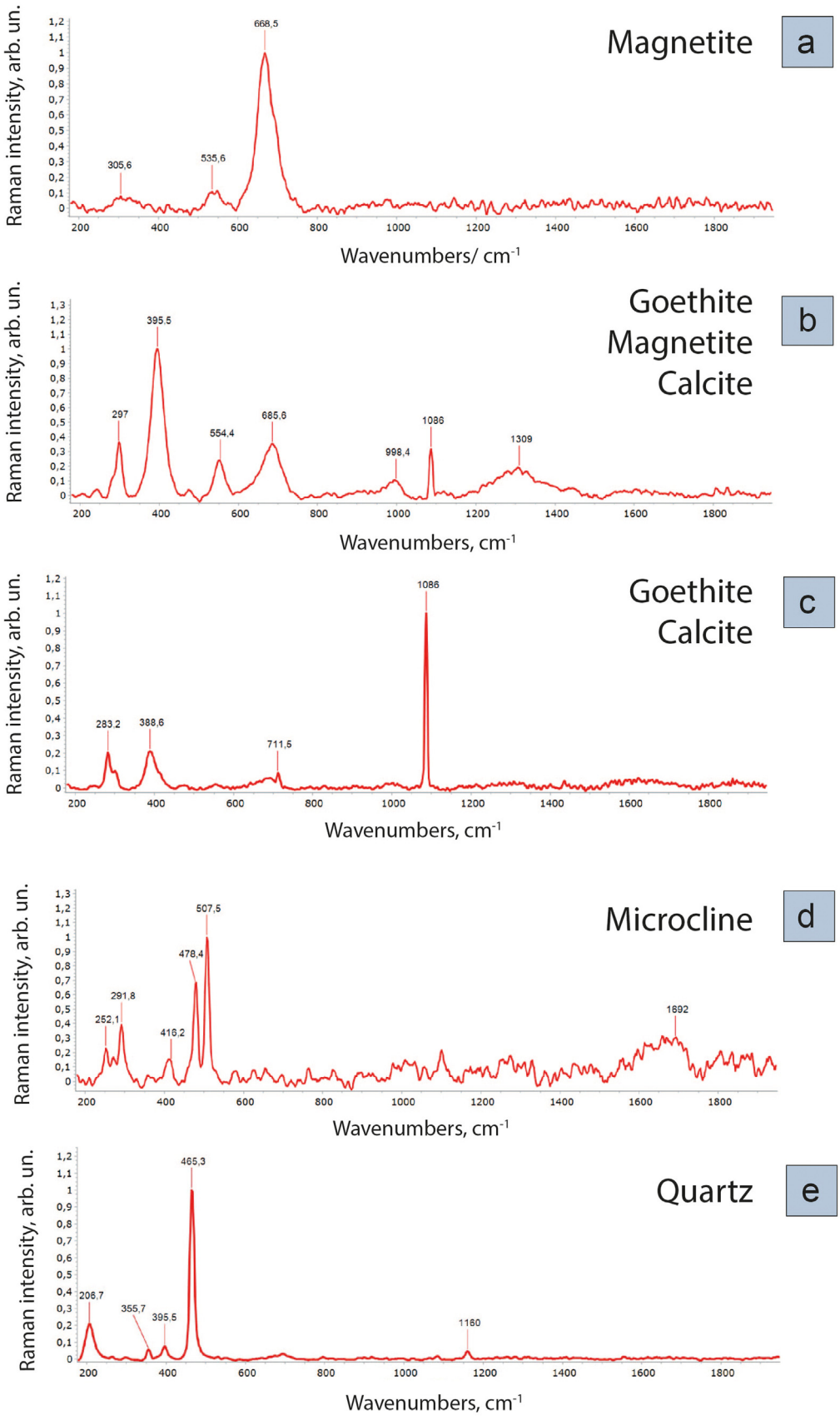

Fig. 8. Raman spectra of sample MC.03.43 (a) magnetite, (b) goethite, magnetite, calcite, (c) goethite, calcite (d) microcline, (e) quartz.

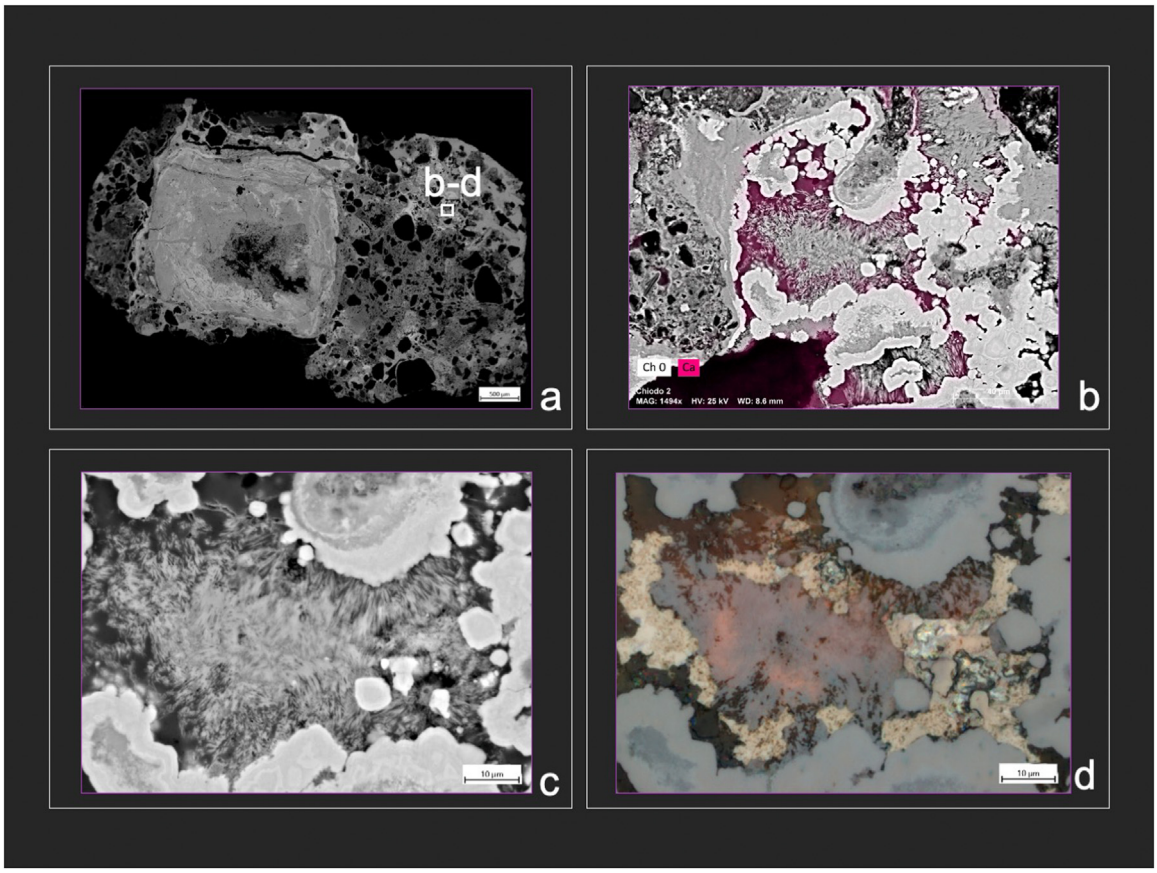

Fig. 9. (a)Reconstruction of MC.03.43 section by ZEN CONNECT and location of targeted areas of interest (b)EDX map of Ca superimposed on BSE image showing secondary calcite formation inside internal gaps in the iron structure (c,d) CLEM images showing detail of calcite crystals.

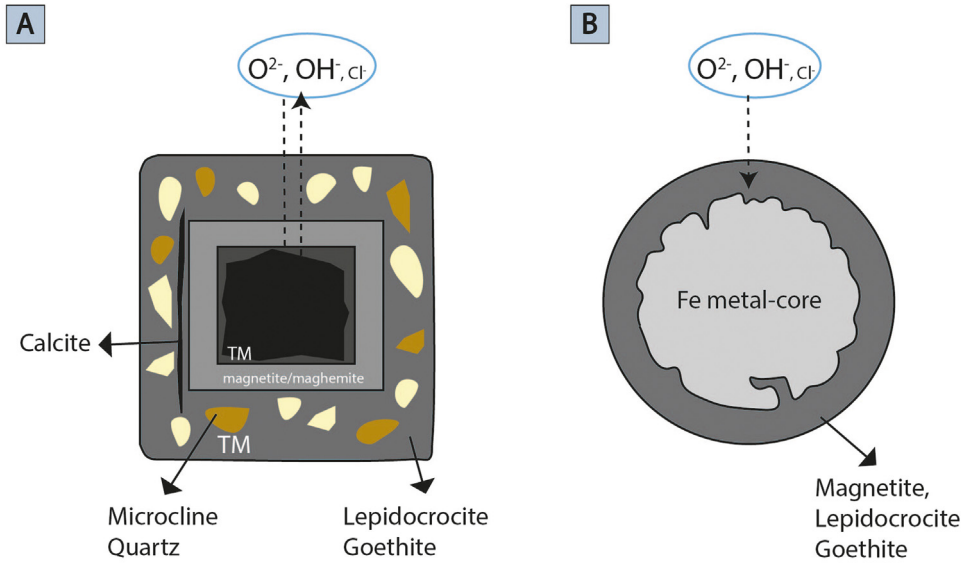

Fig. 10. Schematic representation of corrosion pattern of iron nails: Model A corresponds to iron nail MC.03.43; Model B represents nail MC.14.08.

that isolate the metal from the surrounding environment, thus reducing the reactivity with chloride. This explains why chloride iron compounds have not been found in most of the iron artifacts from Motya [9,10].

At the same time, in alkaline conditions, the solubility of iron oxides and oxyhydroxides increases due to the presence of OH^- ions, and these minerals can dissolve and release iron ions (Fe^{3+}). The dissolved iron ions can then react with OH^- ions to form insoluble iron hydroxides or oxyhydroxides.

This approach, which combines XRM, LM, SEM, and micro-Raman spectroscopy, has proven particularly valuable in unraveling the complex micro-chemistry and structure of ancient artifacts. By integrating multiple techniques, it overcomes the limitations of individual methods, offering a more comprehensive understanding of

the sample. Correlative light and electron microscopy (CLEM) plays a pivotal role in this approach, leveraging the qualities of both light and electron microscopy through unique software to generate composite images. This combination brings together the high resolution of electron microscopy with the wide field of view afforded by light microscopy. While LM provides valuable insights into the morphology of corrosion layers, grain structure, inclusions, and defects, albeit with limited resolution, SEM enables the identification of fine-scale features such as grain boundaries and inclusions and the elemental analysis through energy-dispersive X-ray spectroscopy (EDS), shedding light on the chemical composition of specific regions within the sample.

Moreover, XRM contextualizes this information in three dimensions, offering precise insights on the structure and evolution of corrosion and fractures in hidden parts of the object. Concurrently, micro-Raman spectroscopy, which is based on the vibrational modes associated with chemical bonds within the sample, serves as a powerful tool for identifying corrosion products. For instance, it discerned between different polymorphs of iron oxyhydroxides, providing valuable insights into the corrosion system.

6. Conclusion

In conclusion, correlative imaging techniques including XRM, CLEM, micro-Raman spectroscopy have provided valuable insights into the corrosion behavior of ancient iron nails from the Phoenician-Punic site of Motya. The integration of complementary information from these techniques allowed for a comprehensive examination of the microstructure and composition resulting from stress corrosion. A comparison between two wrought iron nails reveals a very different evolution of corrosion depending upon the manufacturing process involved. The conclusions obtained are summarized as follows:

1. Nail MC.14.08 exhibited a well-preserved iron core covered by a thin layer of oxyhydroxides. The presence of goethite, lepidocrocite, and sporadic regions of magnetite indicated an ongoing corrosion process. In contrast, nail MC.03.43 displayed extensive corrosion, with two distinct corrosion layers: a dense corrosion layer and a transformed medium containing precipitated iron corrosion phases intermixed with elements from the surrounding soil. Micro-Raman spectroscopy also identified a complex mixture of soil minerals embedded within the nail.
2. Furthermore, three-dimensional imaging using X-ray microscopy allowed for the visualization of internal structures and the reconstruction of the original shape of the nails. The presence of cracks observed in nail MC.03.43 suggested that it had undergone repeated mechanical stress during the forging process. In contrast, nail MC.14.08 exhibited a homogeneous and well-preserved iron core, indicating limited exposure to external forces and environmental factors.

Acknowledgments

Nails have been uncovered by the Sapienza Archaeological Expedition to Motya thanks to the fruitful cooperation with the Superintendency of Trapani of the Sicilian Region, and the G. Whitaker Foundation, Palermo. PRIN 2017 Project: “People of the Middle Sea. Innovation and integration in ancient Mediterranean (1600-500 BC)” [B.2. Innovative metallurgy], funded by the Italian Ministry of Education, University and Research provided funding for this research Prot. 2017EYZ727. Financial support was also provided by Sapienza University of Rome (Great Excavation Funds; Ateneofunding). This work has been partially funded by ATOM project (Advanced TOmography and Microscopies) granted by Regione Lazio with the call “Open Infrastructure for research” (G11949, 04.09.2017) 2017.

Supplementary materials

Supplementary material associated with this article can be found, in the online version, at doi:10.1016/j.culher.2024.04.016.

References

[1] F. Cognigni, L. Miraglia, S. Contessi, F. Biancardi, M. Rossi, Correlative light and electron microscopy (CLEM): a multifaceted tool for the study of geological specimens, (2023) 74–85.
[2] R.L. Mitchell, P. Davies, P. Kenrick, T. Volkenandt, C. Pleydell-Pearce, R. Johnston, Correlative microscopy: a tool for understanding soil weathering in modern analogues of early terrestrial biospheres, Sci. Rep. 11 (2021) 1–14, doi:10.1038/s41598-021-92184-1.
[3] D.L. Sexton, S. Burgold, A. Schertel, E.I. Tocheva, Super-resolution confocal cryo-CLEM with cryo-FIB milling for in situ imaging of Deinococcus radiodurans, Curr. Res. Struct. Biol. 4 (2022) 1–9, doi:10.1016/j.crstbi.2021.12.001.
[4] T.L. Burnett, S.A. McDonald, A. Gholinia, R. Geurts, M. Janus, T. Slater, S.J. Haigh, C. Ornek, F. Almuaili, D.L. Engelberg, G.E. Thompson, P.J. Withers, Correlative tomography, Sci. Rep. 4 (2014) 1–6, doi:10.1038/srep04711.
[5] Y. Salem, O. Oudbashi, D. Eid, Characterization of the microstructural features and the rust layers of an archaeological iron sword in the Egyptian Museum in Cairo (380–500 A.D.), Herit. Sci. 7 (2019) 1–12, doi:10.1186/s40494-019-0261-2.
[6] D. Neff, S. Reguer, L. Bellot-Gurlet, P. Dillmann, R. Bertholon, Structural characterization of corrosion products on archaeological iron: an integrated analytical approach to establish corrosion forms, J. Raman Spectrosc. 35 (2004) 739–745.
[7] L. Selwyn, Overview of archaeological iron: the corrosion problem, key factors affecting treatment, and gaps in current knowledge, Proc. Met. (2004) 294–306.
[8] Y.T. He, S.J. Traina, Transformation of magnetite to goethite under alkaline pH conditions, Clay Miner. 42 (2007) 13–19.
[9] M. Bernabale, F. Cognigni, L. Nigro, M. Rossi, T. De Caro, C. De Vito, A comprehensive strategy for exploring corrosion in iron – based artefacts through advanced Multiscale X – ray Microscopy, Sci. Rep. 12 (2022) 1–9, doi:10.1038/s41598-022-10151-w.
[10] M. Bernabale, F. Cognigni, C. Mancini, A. Proietti, F. Mura, D. Montanari, L. Nigro, M. Rossi, C. De Vito, 3D fractures analysis and conservation assessment of wrought iron javelin through advanced non – invasive techniques, Sci. Rep. 13 (2023) 1–11, doi:10.1038/s41598-023-37179-w.
[11] H.J. Simon, G. Cibin, C. Reinhard, Y. Liu, E. Schofield, I.C. Freestone, Influence of microstructure on the corrosion of archaeological iron observed using 3D synchrotron micro-tomography, Corros. Sci. 159 (2019) 31–34, doi:10.1016/j.corsci.2019.108132.
[12] K. Haneca, K. Deforce, M.N. Boone, D. Van Loo, M. Dierick, J. Van Acker, J. Van Den Bulcke, X-ray sub-micron tomography as a tool for the study of archaeological wood preserved through the corrosion of metal objects, Archaeometry 54 (2012) 893–905, doi:10.1111/j.1475-4754.2011.00640.x.
[13] F. Di Turo, G. Moro, A. Artesani, F. Albertin, M. Bettuzzi, D. Cristofori, L.M. Moretto, A. Traviglia, Chemical analysis and computed tomography of metallic inclusions in Roman glass to unveil ancient coloring methods, Sci. Rep. 11 (2021) 1–12, doi:10.1038/s41598-021-90541-8.
[14] M. Jacot-Guillarmod, K. Schmidt-Ott, D. Mannes, A. Kaestner, E. Lehmann, C. Gervais, Multi-modal tomography to assess dechlorination treatments of iron-based archaeological artifacts, Herit. Sci. 7 (2019) 1–14, doi:10.1186/s40494-019-0266-x.
[15] J. Li, P. Guériau, M. Bellato, A. King, L. Robbiola, M. Thoury, M. Baillon, C. Fossé, S.X. Cohen, C. Moulhérat, A. Thomas, P. Galtier, L. Bertrand, Synchrotron-based phase mapping in corroded metals: insights from early copper-base artifacts, Anal. Chem. 91 (2019) 1815–1825, doi:10.1021/acs.analchem.8b02744.
[16] P.J. Withers, D. Grimaldi, C.K. Hagen, E. Maire, M. Manley, A. Du Plessis, X-ray computed tomography, Nat. Rev. Methods Prim. (2021), doi:10.1038/s43586-021-00015-4.
[17] A. Re, J. Corsi, M. Demmelbauer, M. Martini, G. Mila, C. Ricci, X-ray tomography of a soil block: a useful tool for the restoration of archaeological finds, Herit. Sci. 3 (2015) 0–6, doi:10.1186/s40494-015-0033-6.
[18] J. Stelzner, F. Gauß, P. Schuetz, X-ray computed tomography for nondestructive analysis of early Medieval swords, Stud. Conserv. 61 (2016) 86–101, doi:10.1179/2047058414Y.0000000157.
[19] L. Dumont, V. Dupuy, T. Nicolas, C. Pelé-Meziani, G. De Mulder, The protohistoric sword from Le Gué-de-Velluire (Vendée, France): a pasticcio's history unveiled by archaeometrical research, J. Archaeol. Sci. Rep. 34 (2020), doi:10.1016/j.jasrep.2020.102645.
[20] X. Zhang, Y. Lei, Q. Cheng, G. Zhou, Application of Computed Tomography in the analysis of the manufacture of eye beads technique, Microchem. J. 156 (2020) 104798, doi:10.1016/j.microc.2020.104798.
[21] M. Jacot-Guillarmod, O. Rozenbaum, V. L'Hostis, P. Dillmann, D. Neff, C. Gervais, Degradation mechanisms of reinforcing iron rebars in monuments: the role of multiscale porosity in the formation of corrosion products investigated by X-ray tomography, J. Anal. At. Spectrom. 30 (2015) 580–587, doi:10.1039/c4ja00388h.
[22] S.M. Ghahari, A.J. Davenport, T. Rayment, T. Suter, J.P. Tinnes, C. Padovani, J.A. Hammons, M. Stampanoni, F. Marone, R. Mokso, In situ synchrotron X-ray micro-tomography study of pitting corrosion in stainless steel, Corros. Sci. 53 (2011) 2684–2687, doi:10.1016/j.corsci.2011.05.040.

[23] N. Yucel, A. Kalkanli, E.N. Caner-Saltik, Investigation of atmospheric corrosion layers on historic iron nails by micro-Raman spectroscopy, J. Raman Spectrosc. 47 (2016) 1486–1493, doi:10.1002/jrs.5014.
[24] D.L.A. De Faria, S. Venâncio Silva, M.T. De Oliveira, Raman microspectroscopy of some iron oxides and oxyhydroxides, J. Raman Spectrosc. 28 (1997) 873–878.
[25] D. Neff, L. Bellot-Gurlet, P. Dillmann, S. Reguer, L. Legrand, Raman imaging of ancient rust scales on archaeological iron artefacts for long-term atmospheric corrosion mechanisms study, J. Raman Spectrosc. An Int. J. Orig. Work All Asp. Raman Spectrosc. Incl. High. Order Process. Also Brillouin Rayleigh Scatt. 37 (2006) 1228–1237.
[26] S.C. Wu, T.Q. Xiao, P.J. Withers, The imaging of failure in structural materials by synchrotron radiation X-ray microtomography, Eng. Fract. Mech. 182 (2017) 127–156, doi:10.1016/j.engfracmech.2017.07.027.
[27] T. Rodet, F. Noo, M. Defrise, The cone-beam algorithm of Feldkamp, Davis, and Kress preserves oblique line integrals, Med. Phys. 31 (2004) 1972–1975.
[28] D. Neff, S. Reguer, L. Bellot-Gurlet, P. Dillmann, R. Bertholon, Structural characterization of corrosion products on archaeological iron: an integrated analytical approach to establish corrosion forms, J. Raman Spectrosc. 35 (2004) 739–745, doi:10.1002/jrs.1130.
[29] D. Neff, P. Dillmann, L. Bellot-Gurlet, G. Beranger, Corrosion of iron archaeological artefacts in soil: characterisation of the corrosion system, Corros. Sci. 47 (2005) 515–535, doi:10.1016/j.corsci.2004.05.029.
[30] M. Bernabale, D. Montanari, L. Nigro, F. Spagnoli, C. Vaccaro, N. Eftekhari, M. Nicoli, C. De Vito, Micro-Raman spectroscopy and complementary techniques applied for the study of copper and iron wastes from Motya (Italy), J. Raman Spectrosc. 54 (2023) 54–67, doi:10.1002/jrs.6453.
[31] M. Hanesch, Raman spectroscopy of iron oxides and (oxy)hydroxides at low laser power and possible applications in environmental magnetic studies, Geophys. J. Int. 177 (2009) 941–948, doi:10.1111/j.1365-246X.2009.04122.x.
[32] S. Dinarelli, F. Mura, C. Mancini, G. La Penna, T. Rinaldi, M. Rossi, Comparison of different correlative AFM-SEM workflows on calcite moonmilk, IOP Conf. Ser. Mater. Sci. Eng. 1265 (2022) 012011, doi:10.1088/1757-899x/1265/1/012011.
[33] O. Petrova, D. Pankin, A. Povolotckaia, E. Borisov, T. Krivul'ko, N. Kurganov, A. Kurochkin, Pigment palette study of the XIX century plafond painting by Raman spectroscopy, J. Cult. Herit. 37 (2019) 233–237, doi:10.1016/j.culher.2018.11.010.
[34] M. Kylafi, A. Katakos, S. Boyatzis, E. Palamara, N. Zacharias, Characterisation and analysis of metallic artefacts from the pylos archaeological museum, Sci. Technol. Archaeol. Res. 3 (2017) 161–168, doi:10.1080/20548923.2018.1456742.
[35] B. Fabbri, S. Gualtieri, S. Shoval, The presence of calcite in archeological ceramics, J. Eur. Ceram. Soc. 34 (2014) 1899–1911, doi:10.1016/j.jeurceramsoc.2014.01.007.
[36] D. Neff, E. Vega, P. Dillmann, M. Descostes, L. Bellot-Gurlet, G. Béranger, Contribution of iron archaeological artefacts to the estimation of average corrosion rates and the long-term corrosion mechanisms of low-carbon steel buried in soil, Corros. Met. Herit. Artefacts (2007) 41–76.
[37] C. Rémazeilles, D. Neff, F. Kergourlay, E. Foy, E. Conforto, E. Guilminot, S. Reguer, P. Refait, P. Dillmann, Mechanisms of long-term anaerobic corrosion of iron archaeological artefacts in seawater, Corros. Sci. 51 (2009) 2932–2941, doi:10.1016/j.corsci.2009.08.022.
[38] A.L. Grevey, V. Vignal, H. Krawiec, P. Ozga, K. Peche-Quilichini, A. Rivalan, F. Mazière, Microstructure and long-term corrosion of archaeological iron alloy artefacts, Herit. Sci. 8 (2020) 1–19, doi:10.1186/s40494-020-00398-9.
[39] S. Polić, S. Ristić, B. Radojković, D. Bajuk-Bogdanović, Corroded medieval iron nail from the Studenica Monastery - Material analysis and laser cleaning, J. Cult. Herit. 66 (2024) 367–374, doi:10.1016/j.culher.2023.12.012.